Airy-Beam-Enabled Binary Acoustic Metasurfaces for Underwater Ultrasound-Beam Manipulation

Zhongtao Hu,[1] Yaoheng Yang,[1] Lu Xu,[1] Yun Jing,[2] and Hong Chen[1,3,*]

[1] *Department of Biomedical Engineering, Washington University in St. Louis, Saint Louis, Missouri 63130, USA*
[2] *Graduate Program in Acoustics, The Pennsylvania State University, University Park, Pennsylvania 16802, USA*
[3] *Department of Radiation Oncology, Washington University School of Medicine, Saint Louis, Missouri 63108, USA*

(Received 12 May 2022; revised 22 June 2022; accepted 13 July 2022; published 26 August 2022)

Airy beams are peculiar beams that are nondiffracting, self-accelerating, and self-healing, and they have offered great opportunities for ultrasound-beam manipulation. However, one critical barrier that limits the broad applications of Airy beams in ultrasound is the lack of simply built devices to generate Airy beams in water. This work presents a family of Airy-beam-enabled binary acoustic metasurfaces (AB BAMs) to generate Airy beams for underwater ultrasound-beam manipulation. AB BAMs are designed and fabricated by three-dimensional (3D) printing with two coding bits: a polylactic acid (which is the commonly used 3D printing material) unit acting as a bit "1" and a water unit acting as a bit "0." The distribution of the binary units on the metasurface is determined by the pattern of Airy beam. To showcase the wave-front engineering capability of the AB BAMs, several examples of AB BAMs are designed, 3D printed, and coupled with a planar single-element ultrasound transducer for experimental validation. We demonstrate the capability of AB BAMs in flexibly tuning the focal region size and beam focusing in 3D space by changing the design of the AB BAMs. The focal depth of AB BAMs can be continuous and electronical tuned by adjusting the operating frequency of the planar transducer without replacing the AB BAMs. The superimposing method is leveraged to enable the generation of complex acoustic fields, e.g., multifoci and letter patterns (e.g., "*W*" and "*U*"). The more complex focal patterns are shown to be also continuously steerable by simply adjusting the operating frequency. Furthermore, the proposed 3D-printed AB BAMs are simple to design, easy to fabricate, and low cost to produce with the capabilities to achieve tunable focal size, flexible 3D beam focusing, arbitrary multipoint focusing, and continuous steerability, which creates unprecedented potential for ultrasound-beam manipulation.

DOI: 10.1103/PhysRevApplied.18.024070

I. INTRODUCTION

The concept of Airy beams originated from quantum mechanics in 1979 [1]. This concept was introduced into optics in 2007 [2], and was later brought into acoustics in 2014 [3]. As a solution of the Schrödinger equation and paraxial wave equation, the Airy function gives rise to Airy beams that are nondiffracting, which means that a beam can propagate for a long distance without significantly extending its width. Simultaneously, this beam laterally shifts in the transverse plane along a parabolic self-accelerating trajectory. When symmetric airy beams are generated, these beams can autofocus at a point. Airy beams also exhibit self-healing properties in the sense that the beams reconstitute themselves and continue their trajectory even after the beam is severely perturbed [4]. Because of these peculiar properties, Airy beams have attracted extensive attention in the past decade and have been applied in a wide range of areas, ranging from particle manipulation [5] and trapping [6], laser filamentation [7], light-sheet microscopy [8], nonlinear optics [9,10], and nondiffracting waveform generation for electron beams and quantum particles [11,12].

Acoustic Airy beams have great potential in acoustic beam manipulation, particle tracking, and acoustic focusing [13–15]; however, one key challenge that hinders the broad application of acoustic Airy beam is the lack of simply built devices to generate these beams. One approach to generate Airy beams is to use phased arrays, which generate desired Airy beams by dynamically modulating the phase delay of each independent transducer element [3,13,16]. Although phased arrays have the advantage of being dynamically programmable, these arrays need a large number of transducer elements individually addressable by complex electronics [17]. Another promising approach is to place an acoustic lens in front of a

*hongchen@wustl.edu

single-element planar transducer. Different design schemes of the acoustic lens have been proposed, such as tailored acoustic phase mask [18], zero-index medium [19], and thermoacoustic phase control [20]. However, these acoustic lens are three-dimensional (3D) materials that can be bulky or complex in design.

Acoustic metasurfaces, which are two-dimensional (2D) materials of subwavelength thickness, offer a great alternative to bulky 3D materials for acoustic wave-front manipulation. Since its inception, the field of acoustic metasurfaces has undergone rapid expansion [21]. Acoustic metasurfaces enable the design of devices with complex and unprecedented functionalities and offer opportunities in many applications, such as beam focusing, cloaking, sound absorption, and anomalous reflection and refraction [22–31]. Among them, beam focusing is one of the most fundamental examples of wave-front engineering. Acoustic focusing is useful not only for fundamental research of wave propagation but also for applied research in fields such as biomedical imaging, therapy, nondestructive testing, and particle manipulation [32–34].

Several acoustic metasurfaces for generating symmetric Airy beams have been manufactured, including the space coiling-up structures [35,36], lossy hole structures [37], and Helmholtz-resonator-like structures [38–40]. However, these pioneering studies focused on airborne sound waves with long wavelengths and often require the manufacturing of subwavelength units with complicated microstructures, which poses challenges to the fabrication for ultrasound since the typical wavelength is on the millimeter scale. Meanwhile, these structures rely mainly on the high acoustic impedance mismatch between air and the solid materials used to build these structures. Hence, the lack of sufficient impedance contrast between water and solid materials prevents the use of these designs for underwater applications [30].

The objective of this work is to develop a family of 3D-printable Airy-beam-enabled binary acoustic metasurfaces (AB BAMs) to enable a broad range of applications in ultrasound-wave manipulations. Binary acoustic metasurfaces have great promise in acoustic wave manipulation by constructing "digital metasurface bits" to acquire sophisticated functions in wave manipulation [41]. Typically, binary acoustic metasurfaces are designed by macroscopically arranging two types of subwavelength meta-atoms with "0" and "1" digital states [42]. Recently, Jiang *et al.* performed theoretical simulations to show that a binary acoustic metasurface could produce Airy beams in water [15]. Their numerical simulations showed the capability of the binary phase modulation in generating ultrasharp focusing Airy beams. In this paper, we propose to develop AB BAMs by a 3D-printing technique using two coding bits, a polylactic acid (PLA) unit acting as the bit "1" and a water unit acting as the bit "0." The distribution of the binary unit on AB BAMs depends on the pattern of Airy beams. By combining numerical simulations with experimental measurements, we demonstrate the versatile capability of the 3D-printed AB BAMs in tuning the focal size, flexible beam focusing in 3D, and generating a complex beam pattern that are continuously steerable along the axial direction.

II. METHODS

A. AB BAM design for single-point focusing

In this section, we provide a full description of how the AB BAM is designed. Considering a circular Airy beam propagating along the z axis, the pressure profile of the Airy beam at the initial plane ($z = 0$) can be described by [43,44]

$$p(x,y) = \mathrm{Ai}\left(\frac{r_0 - \sqrt{(x-x_0)^2 + (y-y_0)^2}}{\omega}\right) \times e^{\left(\alpha\left(r_0 - \sqrt{(x-x_0)^2+(y-y_0)^2}/\omega\right)\right)}, \quad (1)$$

where $\mathrm{Ai}(s) = 1/\pi \int_0^\infty \cos(t^3/3 + st)dt$ is the Airy function, r_0 is a ring parameter related to the radial position of the primary Airy ring and ω is the radial scaling factor, (x, y) represent the coordinates on the initial plane of the metasurface, and the circle center (x_0, y_0) decides the center of the initial plane of Airy beam, which directly defines the focused position of the AB BAM in the x-y plane. In addition, the term α is an exponential decay factor in ensuring that the wave conveys finite energy, it affects only the amplitude, but does not affect the phase distribution of the Airy beam ($\alpha = 0.002$ for all designs in this study henceforth). As an example, the phase extraction in Fig. 1(b) shows the cross sections of the Airy-beam profiles generated by three different exponential decay factors: $\alpha_1 = 0.002$, $\alpha_2 = 0.05$, and $\alpha_3 = 0.1$. We can see that the decay factor affects only the amplitude of the Airy-beam pattern, but not the phase profile. The set of parameters (r_0, ω) are named as property parameters, which determine the focal properties of the AB BAM, including the focal depth (z_0), full length of half maximum (FLHM) and FWHM.

Figures 1(a)–1(d) show the steps taken to design the AB BAM for single-point focusing. First, the amplitude $p(x,y)$ distribution of the Airy beam at its initial plane is calculated. The cross-section line of $p(x,y)$ exhibits an oscillatory and exponential decaying nature with $p(x,y) = 0$ being the turning point [Fig. 1(a)]. Second, the pressure profile is converted to a binary phase with $\varphi(x,y) = 0$ for $p(x,y) > 0$ and $\varphi(x,y) = \pi/2$ for $p(x,y) < 0$ [Figs. 1(b) and 1(c)]. Third, the binary phase map is rendered into a 3D-printed model for the design of a circular-shape AB BAM [Fig. 1(d)]. Finally, the 3D model is printed using a 3D printer (Ultimaker S5, Ultimaker, Netherlands)

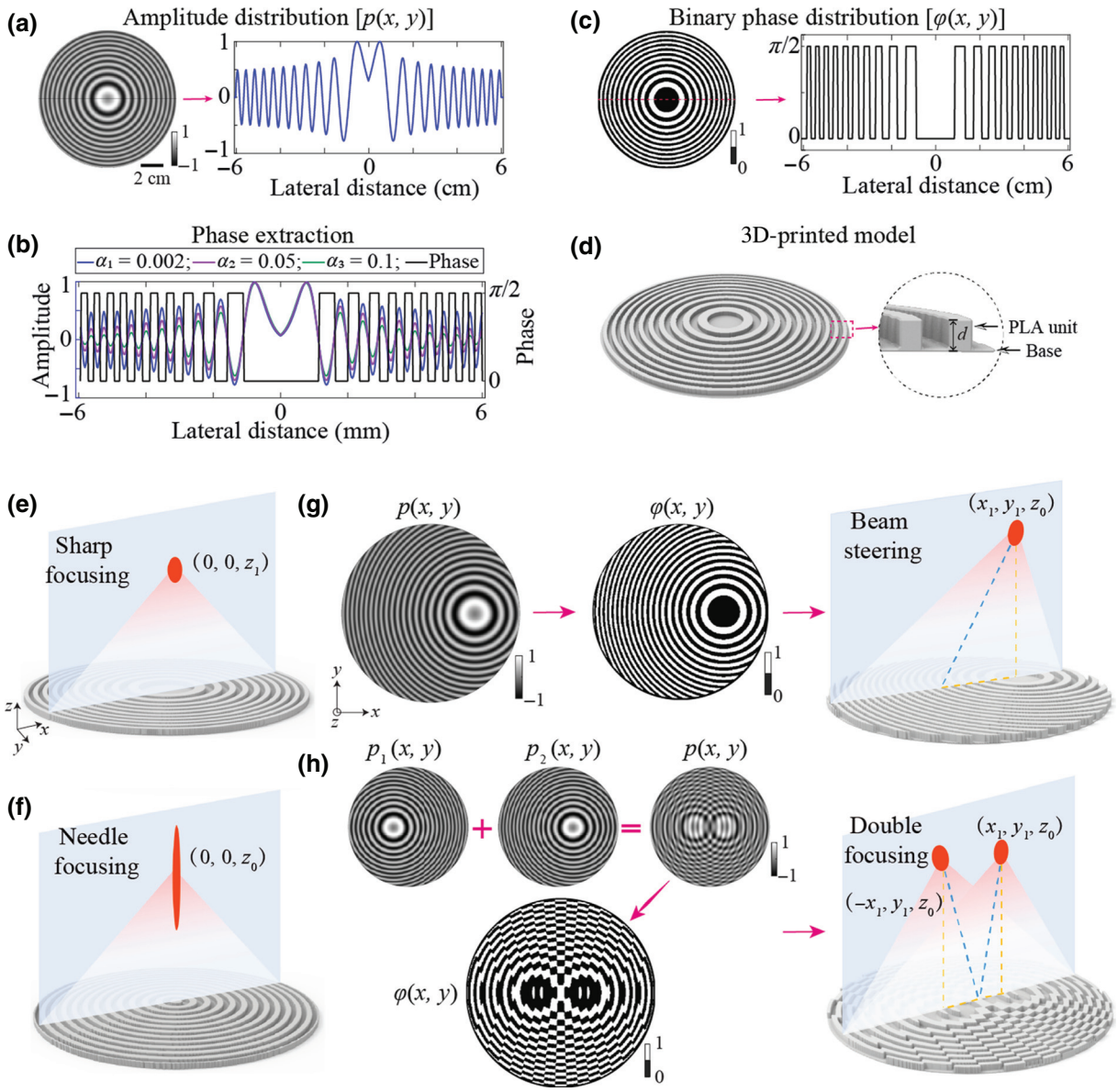

FIG. 1. Design of 3D-printed AB BAMs. (a) AB BAM is designed based on the Airy-beam amplitude distribution $p(x,y)$ at the initial plane with the beam's cross-section line of the amplitude shown on the right side. (b) The term α is an exponential decay factor that affects only the amplitude, but does not affect the phase distribution of the Airy beam. After phase extraction, the pressure distribution is converted into a binary phase profile $\varphi(x,y)$ with the profile's cross-section line of the amplitude shown on the right side (c). (d) The black and white circles represent units "1" and "0," respectively. The phase profile is then converted to a 3D model of an acoustic metasurface with the metasurface's thickness d chosen to generate a phase delay of $\pi/2$. The 3D model is made with a 3D printer using polylactic acid (PLA) filament. The AB BAM can be designed to tune the focusing property. For example, the AB BAM can generate a focused ultrasound beam with sharp focusing (e) and needle focusing (f). (g) Illustration of the AB BAM designed for off-axis beam focusing. (h) Illustrations of AB BAM designed for multipoint focusing. Superimposing the patterns of Airy beams focused at one point on the left $[p_1(x,y)]$ and one point on the right $[p_2(x,y)]$ to construct the amplitude distribution of double focusing $[p(x,y)]$. The amplitude profile is converted to a binary pattern $\varphi(x,y)$ and 3D printed to generate a double-focusing beam.

using the polylactic acid plastic as the filament at printing resolutions of 0.25 and 0.01 mm for the surface and layer, respectively. We couple the printed AB BAM with a planar single-element ultrasound transducer with a center frequency of 500 kHz and an aperture of 120 mm. In addition, the AB BAM has a diameter of 120 mm to match the aperture of the transducer.

The phase delay of each pixel on the metasurface is proportional to its thickness [45]. To produce a phase delay of $\pi/2$, the thickness of unit "1" (d) is

calculated using $(2\pi f/c_1)d - (2\pi f/c_2)d = \pi/2$, where c_1 and c_2 are the sound speed of the water and polylactic acid, respectively, and f is the operating frequency. Thus, the thickness is represented as $d = c_1c_2/4f\,(c_2 - c_1)$. The pressure transmission coefficient (T) of each unit "1" can be calculated using [46] $T = 2Z_r/(2Z_r\cos(2\pi fd/c_2) - i(Z_r^2 + 1)\sin(2\pi fd/c_2))$, where the normalized acoustic impedance is given by $Z_r = Z_2/Z_1$, the impedance of water is given by $Z_1 = \rho_1c_1$, and the impedance of polylactic acid is given by $Z_2 = \rho_2c_2$. The terms ρ_1 and ρ_2 are the densities of water and polylactic acid, respectively.

The acoustic properties of polylactic acid material are obtained experimentally using a pulse-echo technique in a cubic structure, resulting in a measured sound speed of 2212 m/s, and a density of 1223 kg/m^3, and absorption of 3.54 dB/cm for 500 kHz. These meausrments matched those reported in previous studies [47,48]. Water as the surrounding medium has a sound speed of 1484 m/s and mass density of 998 kg/m^3 at room temperature. The thickness of the AB BAM is calculated to be 2.35 mm for a 500-kHz transducer, which is approximately 0.8λ ($\lambda = 2.97$ mm). The metasurface includes two printed parts. The first part is the polylactic acid unit on the metasurface with a depth of 2.25 mm that provides $\pi/2$ phase shift for the 500-kHz transmitted ultrasonic wave. The second portion is the base plate printed at a thickness of 0.10 mm, which is needed to stabilize the metasurface. The transmission coefficient is 99.6% for unit "1," which indicates efficient transmission through the metasurface.

The designed AB BAMs enable flexible and versatile ultrasound-beam manipulations. In this study, we demonstrate that AB BAMs can achieve tunable focusing properties, flexible beam focusing, arbitrary multipoint focusing, and continuous steering. We can achieve a sharp-focused beam [Fig. 1(e)] with a small FLHM and a large FWHM and a needle-focused beam [Fig. 1(f)] with a large FLHM and a small FWHM. The focus of the Airy beams can be steered along the center axis of the metasurface. Moreover, the focus can be steered off axis by moving the ring center (x_0, y_0) from the geometric center (0, 0) to off center $(x_m, y_m) \neq (0, 0)$. As illustrated in Fig. 1(g), the amplitude profile of an Airy beam centered at (x_1, y_1) is calculated and then transformed into a binary phase profile for off-axis steering. The focus of the AB BAM can also be tuned continuously along propagation direction by adjusting the operating frequency of the planar transducer without replacing the AB BAMs.

B. AB BAM design for multipoint focusing

In addition to single-point focusing, AB BAMs can be designed to generate multifocal points through the superimposing method [49]. The final amplitude map $p(x,y)$ can be expressed as

$$p(x,y) = \sum_m p_m(x,y), m = 1, 2, \ldots, \tag{2}$$

$$p_m(x,y) = \mathrm{Ai}\left(\frac{r_0 - \sqrt{(x-x_m)^2 + (y-y_m)^2}}{\omega}\right) \times e^{\left(\alpha\left(r_0 - \sqrt{(x-x_m)^2+(y-y_m)^2}/\omega\right)\right)}.$$

As a demonstration of this capability, we design AB BAMs for double focusing and generating patterns of "*W*" and "*U*." For the generation of two foci, the amplitude distribution $p(x,y)$ at the initial plane is calculated by the superposition of the Airy-beam patterns with two foci [$p_1(x,y)$ and $p_2(x,y)$], as illustrated in Fig. 1(h). The superimposed amplitude map $p(x,y)$ is transformed into a binary phase map $\varphi(x,y)$ to generate an ultrasound field with double focusing. The superposition method can be extended to form arbitrary focusing patterns in space, such as the letters "*W*" and "*U*."

C. Numerical simulation and experimental validation

Several examples of AB BAMs are designed and 3D printed to showcase the wave-front engineering capability of the AB BAMs. We perform numerical simulations and experimental measurements to validate the performance of the 3D-printed AB BAMs.

Numerical simulations of the 3D acoustic pressure fields generated by the AB BAMs that are coupled with a planar and uniform incident wave is performed using an open-source MATLAB toolbox, *k* wave, and pseudospectral method with *k*-space dispersion correction [50–53]. Cluster computing with one graphics processing unit (Nvidia Tesla V100, Nvidia Corporation, Santa Clara, CA, USA) is used to accelerate the 3D simulations. A numerical grid with a spatial step of $\Delta x = \Delta y = \Delta z = 200$ μm and a numerical temporal step of $\Delta t = 20$ ns are used, which leads to a Courant-Friedrichs-Lewy number of 0.1 and a spatial sampling of approximately 15 grid points per wavelength in water for a frequency of 0.5 MHz. These parameters are fixed for all simulations in this study.

Experimental validation is carried out by coupling the 3D-printed metasurfaces with the 500-kHz ultrasound transducer. The ultrasound transducer is made of a single-element circular lead zirconate titanate (PZT) ceramic (DL-20, Del Piezo Specialties LLC, West Palm Beach, FL, USA). Two wires are soldered to the two electrodes of the transducer and connected to an electrical driving system composed of a function generator (Model 33500B, Keysight Technologies Inc., Englewood, CO, USA) and a power amplifier (1020L, Electronics & Innovation, Rochester, NY, USA). The transducer is mounted

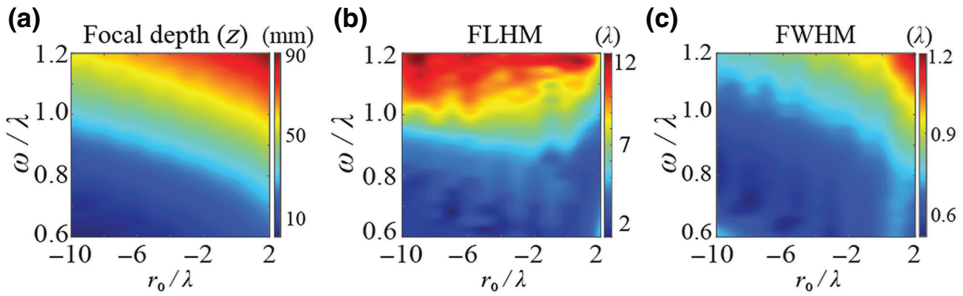

FIG. 2. Tunable focusing properties of AB BAMs. The operating frequency is 500 kHz, r_0/λ is within the range of $[-10, 2]$, and ω/λ is within the range of [0.6, 1.2]. The simulation results show that (a) the focal depth is tunable from 0.1 to 90.0 mm, (b) the FWHM is tunable from 1.33λ to 12.61λ, and (c) the FWHM is tunable from 0.51λ to 1.20λ.

in a 3D-printed housing. The ultrasound pressure fields are measured using a lipstick hydrophone (HGL-200, ONDA Corporation, Sunnyvale, CA, USA) in a water tank filled with degassed and deionized water at 22°. The hydrophone is connected to a preamplifier (AG-20X0, Onda Corp., Sunnyvale, CA, USA) and a digital oscilloscope (Picoscope 5443D, St. Neots, United Kingdom) and is moved in 3D using a computer-controlled 3D stage (PK245-01AA, Velmex Inc., NY, USA). The 3D stage is controlled to move at a step size of 0.3 mm over a scanning volume that covers the focal patterns of the ultrasound fields. The calibration is conducted by driving the ultrasound transducer with a 20-cycle pulsed wave with a pulse repetition frequency of 100 Hz.

III. RESULTS

A. Tunable focusing properties

The focusing properties of AB BAMs, which include focal depth, FLHM, and FWHM, are tunable by modulating the property parameters (r_0, ω). Over a selected parameter space with r_0/λ in the range of $[-10, 2]$ and ω/λ in the range of [0.6, 1.2], numerical simulations show that the focal depth of the ultrasound beam can be tuned from 0.1 to 90 mm [Fig. 2(a)], FLHM can vary from 1.33λ to 12.61λ [Fig. 2(b)], and FWHM can change from 0.51λ to 1.20λ [Fig. 2(c)]. The numerical results highlight the flexibility of AB BAMs in tuning the focusing properties.

Two AB BAMs are 3D printed to demonstrate the unique capability of AB BAMs in tuning the focusing properties. These two metasurfaces are designed to achieve sharp and needle focusing at the same focal depth $z = 45$ mm, respectively. Figures 3(a) and 3(b) show the designed and 3D-printed AB BAMs. The sharp focused beam is designed with ($r_0 = 1.73$, $\omega = 0.89$), and the needle-focused beam is designed with ($r_0 = -9.00$, $\omega = 1.10$). The simulated and measured ultrasound fields in the axial plane are presented in Figs. 3(c) and 3(d) and the ones for the lateral plane are presented in Figs. 3(e) and 3(f). The axial and lateral beam profiles across the focal point are shown in Fig. 3(g). Numerical simulation finds that the sharp focused beam has a short focal length with a FLHM of 3.36λ and FWHM of 0.81λ. The needle-focused beam has an elongated focal region with a FLHM of 11.15λ and FWHM of 0.69λ. On the other hand, the experimental results show that the FLHM and FWHM are 3.42λ and 0.83λ for the sharp-focused beam and 10.96λ and 0.72λ for the needle-focused beam. The numerical simulation and experimental measurements are in good agreement. These two examples demonstrate that the focusing properties of AB BAMs are highly tunable by modulating the pattern of Airy beams. Different focusing patterns can be used for various ultrasound applications. For example, high-intensity focused ultrasound (HIFU) therapy requires a beam with a short axial length to avoid off-target effects in the surrounding tissue [54], whereas ultrasound imaging requires a beam with narrow lateral focal dimensions to improve the lateral imaging resolution [55].

B. Flexible beam focusing in 3D

AB BAMs have the capability to flexibly adjust their foci in 3D space by changing the design parameters. We design and 3D print several AB BAMs to demonstrate this capability. Figure 4(a) shows the designed and 3D-printed AB BAMs for beam focusing along the center axis of the metasurface. Three AB BAMs are designed using different sets of property parameters ($r_0 = 1.38$, $\omega = 0.83$), ($r_0 = 1.73$, $\omega = 0.89$), and ($r_0 = 1.98$, $\omega = 0.97$) to achieve focal depths of $z = 35$ mm, $z = 45$ mm, and $z = 55$ mm, respectively. Figure 4(b) displays the simulated and measured ultrasound fields on the *x*-*z* plane. The corresponding normalized axial and lateral focal beam profiles for each focal depth are presented in Fig. 4(c). Both the FWHM and FLHM slightly increase as the focal depth increases. Based on the simulation results, the FWHMs are 0.74λ, 0.81λ, and 0.88λ, and the FLHMs are 2.74λ, 3.36λ, and 4.42λ for the focal depths of $z = 35$ mm, 45 mm, and 55 mm, respectively. The corresponding experimental results find that the corresponding FWHMs are 0.79λ, 0.83λ, and 0.93λ, and the FLHMs are 3.02λ, 3.42λ, and 4.45λ. The

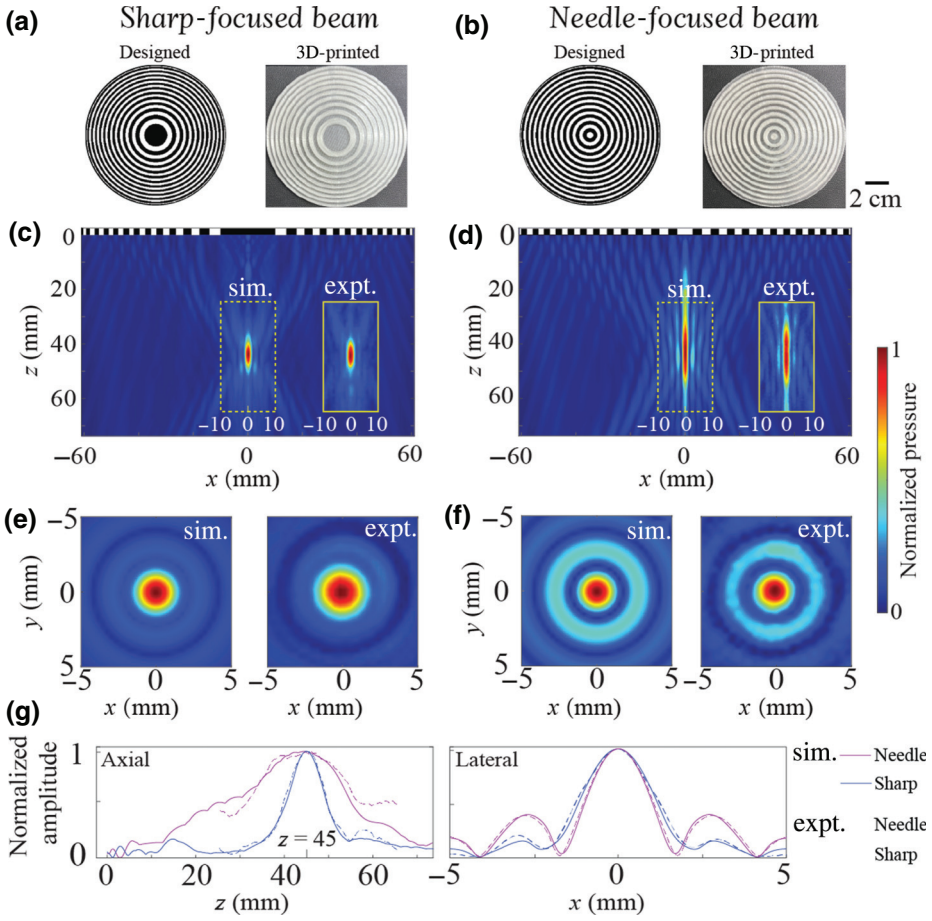

FIG. 3. Two examples to demonstrate the tunable focusing properties of AB BAMs. AB BAMs for (a) sharp-focused beam ($r_0 = 1.73, \omega = 0.89$), and (b) needle-focused beam ($r_0 = -9.00, \omega = 1.10$) at a focal depth $z = 45$ mm are designed (left) and 3D printed (right). Simulated (sim.) and experimental (expt.) measured ultrasound pressure fields in the axial x-z plane are shown for (c) sharp-focused beam and (d) needle-focused beam. The corresponding ultrasound fields in the lateral x-y plane are presented for the (e) sharp-focused beam and (f) needle-focused beam. The pressure fields are normalized to the peak pressure. (g) Simulated and experimentally measured axial and lateral focal beam profiles across the focal point for sharp- and needle-focused beams. The measured peak pressure of sharp- and needle-focused beams are 0.93 and 0.61 MPa, respectively.

experimental measurements match the simulation results and agree well with the design.

Figure 4(d) shows the designed and 3D-printed AB BAMs for off-axis beam focusing. The circle center (x_0, y_0) is set at $(0, 0)$ mm, $(-15, 0)$ mm, and $(-30, 0)$ mm, with a constant focal depth $z = 45$ mm ($r_0 = 1.73$, $\omega = 0.89$), to design three AB BAMs focusing, respectively, at $x = 0$ mm, $x = -15$ mm, and $x = -30$ mm, respectively. Figure 4(e) displays the simulated and measured ultrasound fields on the x-z plane when the focus is steered off axis. The generated acoustic fields accurately match the simulations. Figure 4(f) presents the corresponding normalized axial and lateral beam profiles from the simulations and experiments. As the focused beam steers from 0 mm to -30 mm off axis, the FLHM remains almost the same at approximately 3.36λ in simulations and approximately 3.42λ in experiments, while the FWHM progressively increases and are from 0.81λ, 0.84λ, to 0.97λ in the simulations and 0.83λ, 0.87λ, and 1.02λ in the experiments. The above findings suggest that the focal position of AB BAMs can be adjusted along the axis and off axis. The 3D arbitrarily focusing property of AB BAM makes the metasurface a versatile tool for various applications.

C. Arbitrary multipoint focusing

The previous results demonstrate the flexibility of AB BAMs for single-point focusing. In this subsection, we extend the applications of AB BAMs to achieve arbitrary multipoint focusing.

Figure 5(a) shows the designed and printed bifocal AB BAM for the bilateral focus. The focal points are set to $(x = -15, y = 0, z = 45)$ mm and $(x = 15, y = 0, z = 45)$ mm, respectively, by superimposing the patterns of two Airy beams at the initial plane. Specifically, the two Airy beams are designed with the circle center located at $(x_0 = -15, y_0 = 0)$mm and $(x_0 = 15, y_0 = 0)$mm using the same property parameters ($r_0 = 1.73$, $\omega = 0.89$) at a focal depth of 45 mm, respectively. Figures 5(b) and 5(e) show the ultrasound fields generated in the x-z plane by simulation and experimental measurements, respectively. The lateral ultrasound fields in the x-y plane are shown in Figs. 5(c) and 5(d). Excellent agreement is observed between the simulation and experiments. The lateral and axial beam forms across the focus are shown in Figs. 5(f) and 5(g). Additionally, the FWHM and FLHM from the experiments (0.95λ and 3.64λ, respectively) are in good agreement with the simulations (0.87λ and 3.53λ, respectively).

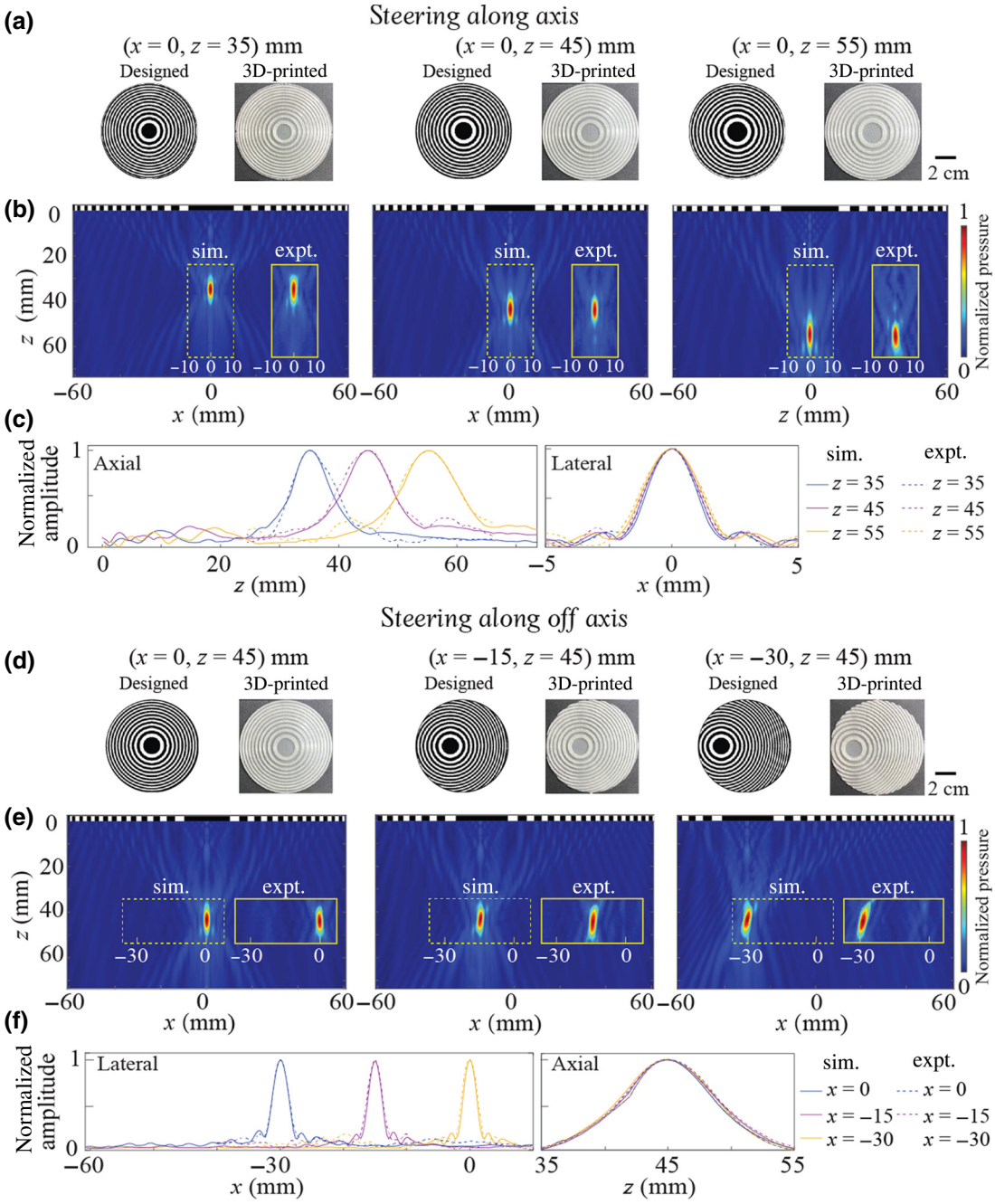

FIG. 4 Flexible focusing in 3D space with AB BAMs. (a) The designed and 3D-printed AB BAM for steering along the axis at $x = 0$ with $z = 35$ mm ($r_0 = 1.38$, $\omega = 0.83$), $z = 45$ mm ($r_0 = 1.73$, $\omega = 0.89$), and $z = 55$ mm ($r_0 = 1.98$, $\omega = 0.97$). (b) The simulated and experimentally measured (offset) ultrasound fields in the x-z plane when steering along the axis with $z = 35$ mm, $z = 45$ mm, and $z = 55$ mm (c) Corresponding normalized axial and lateral beam profiles. The measured peak pressures are 0.81, 0.93 and 0.88 MPa for $z = 35$, 45 and 55 mm, respectively. (d) The designed and 3D-printed AB BAMs for steering off axis at $z = 45$ mm with $x = 0$ mm, $x = -15$ mm, and $x = -30$ mm, respectively. (e) Resulting fields from experiments and simulations when steering along off axis at $z = 45$ mm with $x = 0$ mm, $x = -15$ mm and $x = -30$ mm. (f) Corresponding normalized lateral and axial beam profiles when steering off axis. The measured peak pressures are 0.93, 0.85 and 0.74 MPa for $x = 0$, -15 and -30 mm, respectively.

Complex multipoint patterns such as the letters "*W*" and "*U*" can also be generated by AB BAMs. Figures 6(a) and 6(d) show the designed and printed AB BAMs that generate the letter "*W*" and "*U*" patterns in the focal plane at $z = 35$ mm with the property parameters ($r_0 = 1.38$, $\omega = 0.83$). Figures 6(b) and 6(e) present the simulated acoustic pressure fields at the focal plane, where the letters are distinctly visible. Figures 6(c) and 6(f) show

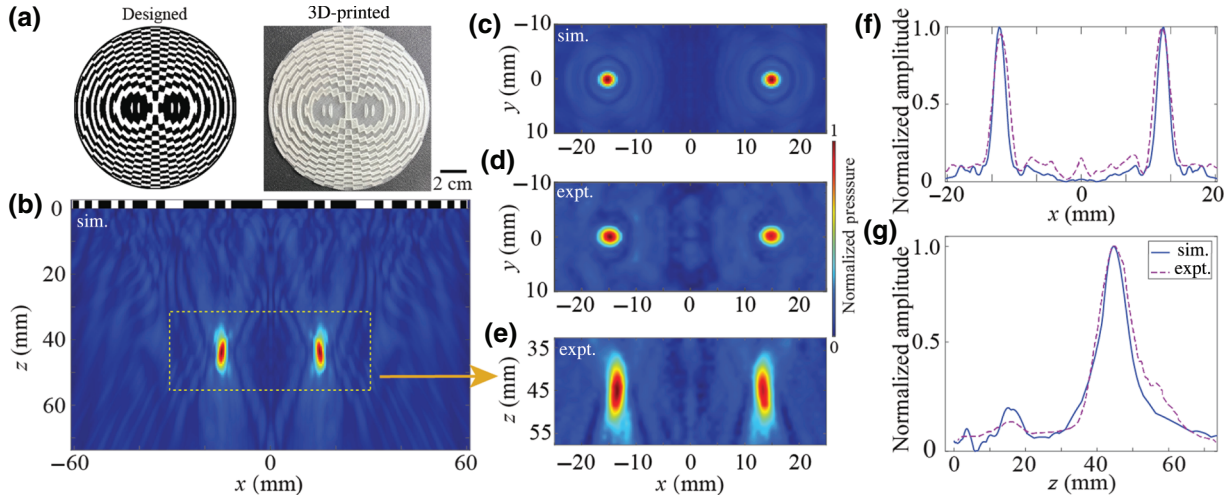

FIG. 5. AB BAM for double focusing. (a) The designed and 3D-printed AB BAM for double focusing at $z = 45$ mm. The ultrasound field in the x-z plane by simulation (b) and experiment (e). (c), (d) Corresponding lateral field in x-z plane. (f), (g) Simulated and experimentally measured axial and lateral pressure profiles. The measured peak pressure is 0.73 MPa.

the experimentally measured ultrasound fields at the focal plane, where both letters are distinctly visible. The simulation and experiment show agreement in the overall shapes of the patterns. The discrepancy between simulation and experiment may be attributed to a slight error in the 3D-printed phase profile caused by fabrication error and shear mode conversion in the PLA material [56]. These examples demonstrate that arbitrary multipoint focusing can be realized by AB BAMs through the superposition method, which can broaden the applications of acoustic Airy beams.

D. Continuously steerable arbitrary pattern focusing

One property of the AB BAM is that it can continuously steer the beam focus along the wave-propagation direction by modulating the operating frequency of the planar transducer without the need to switch the metasurface. In this subsection, we evaluate the continuously steerable properties of the AB BAM by changing its operating frequency for single and multifocal beams.

For single-point focusing, we show that designed and 3D-printed AB BAMs can dynamically tune the focal depth from 28.4 to 41.6 mm by increasing the operating frequencies from 0.45 to 0.55 MHz. This frequency range is within the bandwidth of the planar transducer. A linear relationship ($R^2 > 0.99$) between the focal depth z and the operating frequency is found, as shown in Fig. 7(b). The experimental results agreed well with the numerical results, with an average relative difference between the experiment and simulation of approximately 3%.

AB BAMs can also be used to continuously steer an arbitrary focusing pattern, as demonstrated in Fig. 8. Figures 8(a)–8(c) show that the multifocal point beam with the pattern of the letter "*U*" is steerable to $z = 28.4$ mm, $z = 35.0$ mm, and $z = 41.6$ mm by changing the operating frequency from 0.45, 0.50 to 0.55 MHz, respectively. As shown in Figs. 8(a)–8(c), the letter "*U*" is distinctly visible at $z = 28.4$ mm, $z = 35.0$ mm, and $z = 41.6$ mm when the frequency increases from 0.45, 0.50, to 0.55 MHz, respectively. Overall, the experimental measurements presented

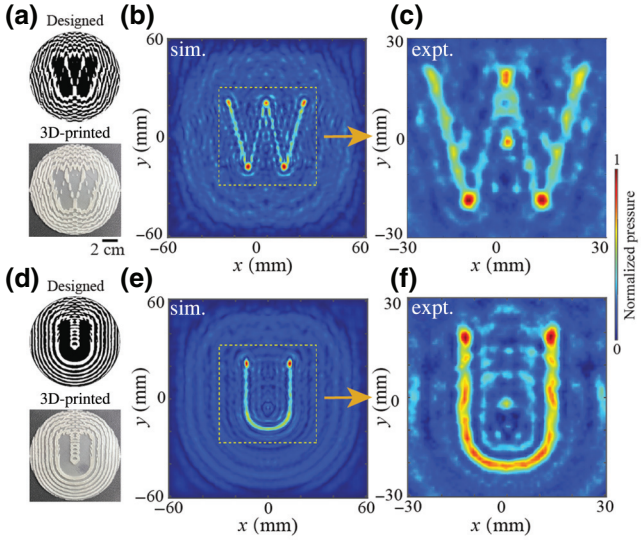

FIG. 6. Multipoint focusing to generate the letters "*W*" and "*U*." (a) The designed and 3D-printed AB BAM to generate the letter "*W*." (b) Simulated and (c) experimentally measured pressure fields with the AB BAM shown in (a). (d) Simulated and 3D-printed AB BAM to generate the letter "*U*." (e) Simulated and (f) experimentally measured pressure fields with AB BAM shown in (d). The focal depth is 35 mm.

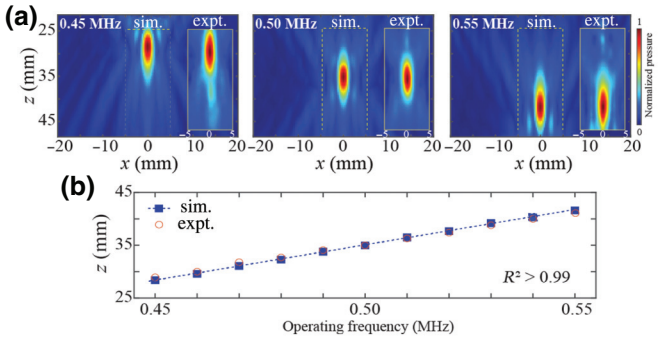

FIG. 7. Electronical steering of a single focusing point by changing the operating frequency. (a) Simulated and experimentally measured ultrasound fields in the x-z plane at 0.45, 0.50, and 0.55 MHz, respectively. (b) Simulated (solid squares) and experimentally measured (open circles) focal depths z_0 from 0.45 to 0.55 MHz. The measured peak pressure varies from 0.82 to 0.98 MPa as the frequency increases from 0.45 to 0.55 MHz.

in Figs. 8(d)–8(f) agree well with the simulation results. Thus, the generated multifocal point beam by AB BAM can work over a broad frequency range and be able to continuously steer by the operating frequency.

IV. CONCLUSION

We design and 3D-print AB BAMs for ultrasound-beam manipulation and demonstrate their capability in ultrasound-beam manipulation in water. AB BAM is a unique binary acoustic lens because it is designed based on Airy beams, which have the peculiar properties of nondiffracting, self-accelerating, and self-healing. Several features of the AB BAM are demonstrated. First, AB BAMs can finely tune the focusing properties such as the FLHM and FWHM by changing the property parameters (r_0, ω) and customizing to various applications. Second, AB BAMs can flexibly adjust the focus in 3D space both along the axis and off axis by modulating the property parameters (r_0, ω) and circle center (x_0, y_0). Third, arbitrary multipoint focusing, such as double focusing and even complex pattern like letters "*W*" and "*U*," can be achieved through the superimposing method, avoiding the application of the iterative method during acoustic hologram design, which can effectively reduce the time consumption. Fourth, the focus of the AB BAM can also be tuned continuously by adjusting the operating frequency for both single-point and multipoint focusing beam.

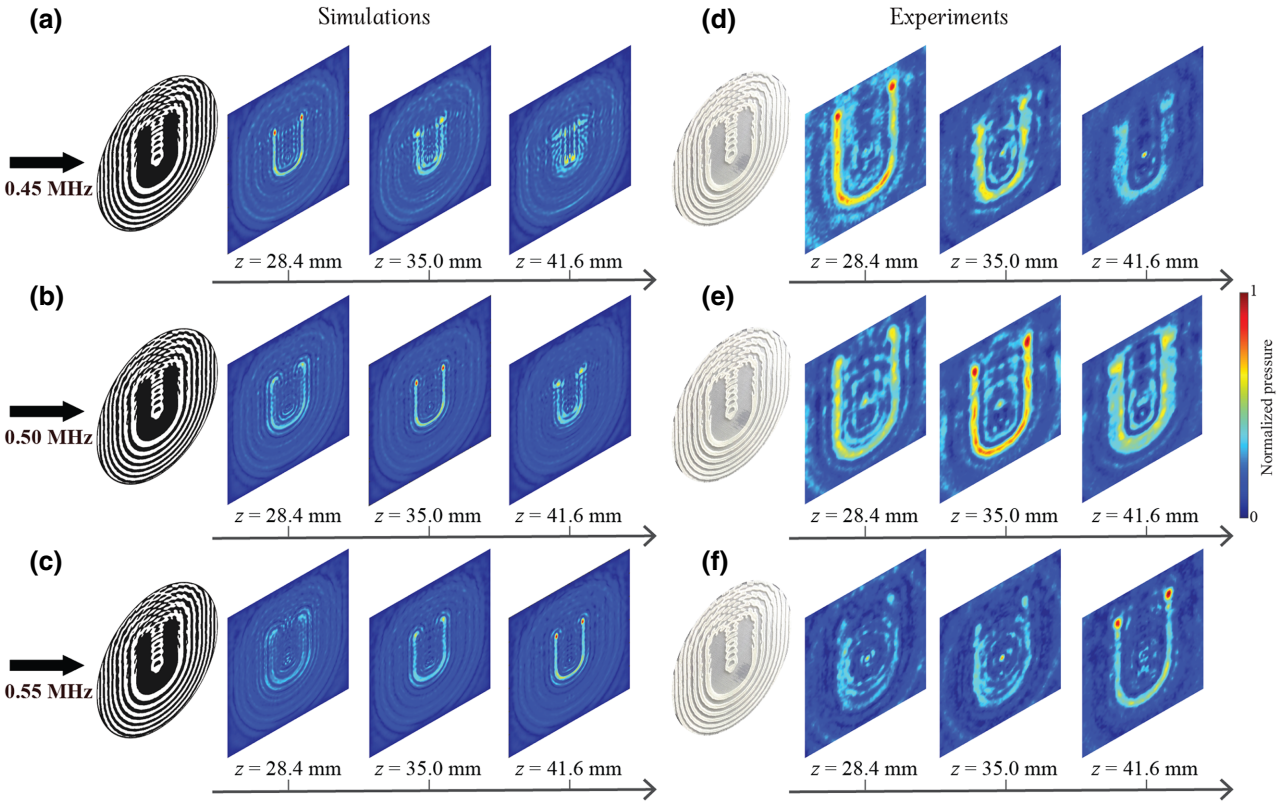

FIG. 8. Electronical steering of the letter "*U*" pattern by changing the operating frequency. Simulated pressure field at depths of 28.4, 35.0, and 41.6 mm by operating frequency of (a) 0.45, (b) 0.50, and (c) 0.55 MHz, respectively. The corresponding experimental pressure field under an operating frequency of (d) 0.45, (e) 0.50, and (f) 0.55 MHz, respectively. Color bar in units normalized to the peak pressure of each operating frequency.

There are several limitations to this study. First, AB BAMs are developed for homogeneous media. The generated ultrasound beams may be distorted in heterogeneous media such as the skull. The potential solution is to design AB BAMs to couple with ultrasound transducers at lower frequencies such as 200 kHz. At such a low frequency, the aberration induced by the skull is not significant. Second, as a proof of concept, our experimental measurements are conducted with the peak pressures <1 MPa. Future studies are needed to investigate the generation of higher pressure levels for applications such as HIFU therapy. The nonlinear effects associated with high-pressure wave propagation will need to be considered when designing the AB BAM for these applications. Last, the focusing properties (FLHM and FWHM) of AB BAMs are highly related to the acoustic properties of the 3D-printing material. This study tests only PLA material. Future work is needed to investigate the performance of AB BAMs printed with other materials.

It is worthwhile to point out that the printing resolution of the 3D printer determines the upper limit of the operating ultrasound frequency of AB BAMs, and the ultrasound frequency determines the spatial resolution of the resultant beam pattern. The practical upper limit of the operating ultrasound frequency depends on the design of each AB BAMs. As an example, the printing resolution (Rs) of the 3D printer used in this study is 0.25 mm. The AB BAM designed for beam focusing shown in Fig. 1(g) has a minimal ring spacing (D) of 1.25 mm for an operating frequency of 0.5 MHz (Freq). Because the AB-BAM design parameter is scaled by the wavelength as shown in Fig. 2, the upper limit of the operating ultrasound frequency ($F_{\max}$) can be calculated as $F_{\max} = (D \times \text{Freq})/\text{Rs}$. As a result, the $F_{\max}$ for the AB BAM shown in Fig. 1(g) is 2.5 MHz.

In conclusion, this study demonstrates that 3D-printed AB BAMs provide a flexible and versatile tool for ultrasound-beam manipulation. It can be easily and accurately manufactured by 3D printing. Complex acoustic patterns can be generated with the AB BAMs coupled with a single-element planar ultrasonic transducer. The proposed 3D-printed AB BAMs can achieve tunable focal region size, flexible focusing in 3D, arbitrary multipoint focusing, and contunious steerablility, which may have the potential for different applications such as neuromodulation [57], HIFU therapy [58,59], ultrasound-mediated microbubbles for blood-brain barrier opening for brain drug delivery [60–63] or enriching the brain tumor-derived molecular biomarkers for sonobiopsy [64–66].

ACKNOWLEDGMENTS

This work is supported in part by the National Institutes of Health Grants (No. R01EB027223, R01EB030102, No. R01MH116981, and No. UG3MH126861). It is also partially supported by the Office of Naval Research (Grant No. N00014-19-1-2335).

[1] M. V. Berry and N. L. Balazs, Nonspreading wave packets, Am. J. Phys. **47**, 264 (1979).
[2] G. A. Siviloglou, J. Broky, A. Dogariu, and D. N. Christodoulides, Observation of Accelerating Airy Beams, Phys. Rev. Lett. **99**, 213901 (2007).
[3] P. Zhang, T. Li, J. Zhu, X. Zhu, S. Yang, Y. Wang, X. Yin, and X. Zhang, Generation of acoustic self-bending and bottle beams by phase engineering, Nat. Commun. **5**, 4316 (2014).
[4] N. K. Efremidis, Z. Chen, M. Segev, and D. N. Christodoulides, Airy beams and accelerating waves: An overview of recent advances, Optica **6**, 686 (2019).
[5] J. Baumgartl, M. Mazilu, and K. Dholakia, Optically mediated particle clearing using Airy wavepackets, Nat. Photonics **2**, 675 (2008).
[6] P. Zhang, J. Prakash, Z. Zhang, M. S. Mills, N. K. Efremidis, D. N. Christodoulides, and Z. Chen, Trapping and guiding microparticles with morphing autofocusing Airy beams, Opt. Lett. **36**, 2883 (2011).
[7] P. Polynkin, M. Kolesik, J. V. Moloney, G. A. Siviloglou, and D. N. Christodoulides, curved plasma channel generation using ultraintense Airy beams, Science **324**, 229 (2009).
[8] T. Vettenburg, H. I. C. Dalgarno, J. Nylk, C. Coll-Lladó, D. E. K. Ferrier, T. Čižmár, F. J. Gunn-Moore, and K. Dholakia, Light-sheet microscopy using an Airy beam, Nat. Methods **11**, 541 (2014).
[9] P. Panagiotopoulos, D. G. Papazoglou, A. Couairon, and S. Tzortzakis, Sharply autofocused ring-Airy beams transforming into non-linear intense light bullets, Nat. Commun. **4**, 2622 (2013).
[10] T. Ellenbogen, N. Voloch-Bloch, A. Ganany-Padowicz, and A. Arie, Nonlinear generation and manipulation of Airy beams, Nat. Photonics **3**, 395 (2009).
[11] I. Kaminer, J. Nemirovsky, M. Rechtsman, R. Bekenstein, and M. Segev, Self-accelerating Dirac particles and prolonging the lifetime of relativistic fermions, Nat. Phys. **11**, 261 (2015).
[12] N. Voloch-Bloch, Y. Lereah, Y. Lilach, A. Gover, and A. Arie, Generation of electron Airy beams, Nature **494**, 331 (2013).
[13] S. Zhao, Y. Hu, J. Lu, X. Qiu, J. Cheng, and I. Burnett, Delivering sound energy along an arbitrary convex trajectory, Sci. Rep. **4**, 6628 (2015).
[14] F. G. Mitri, Airy acoustical–sheet spinner tweezers, J. Appl. Phys. **120**, 104901 (2016).
[15] X. Jiang, Y. Li, D. Ta, and W. Wang, Ultrasonic sharp autofocusing with acoustic metasurface, Phys. Rev. B **102**, 064308 (2020).
[16] K. Mohanty, S. Mahajan, G. Pinton, M. Muller, and Y. Jing, Observation of self-bending and focused ultrasound beams in the megahertz range, IEEE Trans. Ultrason. Ferroelectr. Freq. Control **65**, 1460 (2018).

[17] K. Melde, A. G. Mark, T. Qiu, and P. Fischer, Holograms for acoustics, Nature **537**, 518 (2016).
[18] U. Bar-Ziv, A. Postan, and M. Segev, Observation of shape-preserving accelerating underwater acoustic beams, Phys. Rev. B **92**, 100301 (2015).
[19] H. Gao, Z. Gu, B. Liang, X. Zou, J. Yang, J. Yang, and J. Cheng, Acoustic focusing by symmetrical self-bending beams with phase modulations, Appl. Phys. Lett. **108**, 073501 (2016).
[20] C. Liu, J.-P. Xia, H.-X. Sun, and S.-Q. Yuan, Thermoacoustic focusing lens by symmetric Airy beams with phase manipulations, J. Phys. D: Appl. Phys. **50**, 505101 (2017).
[21] B. Liang, J. Cheng, and C.-W. Qiu, Wavefront manipulation by acoustic metasurfaces: From physics and applications, Nanophotonics **7**, 1191 (2018).
[22] Y. Li, B. Liang, X. Tao, X. Zhu, X. Zou, and J. Cheng, Acoustic focusing by coiling up space, Appl. Phys. Lett. **101**, 233508 (2012).
[23] G. Ma, M. Yang, S. Xiao, Z. Yang, and P. Sheng, Acoustic metasurface with hybrid resonances, Nat. Mater. **13**, 873 (2014).
[24] Y. Li, X. Jiang, R. Q. Li, B. Liang, X. Y. Zou, L. Yin, and J. C. Cheng, Experimental Realization of Full Control of Reflected Waves with Subwavelength Acoustic Metasurfaces, Phys. Rev. Appl. **2**, 064002 (2014).
[25] S.-D. Zhao, A. L. Chen, Y.-S. Wang, and C. Zhang, Continuously Tunable Acoustic Metasurface for Transmitted Wavefront Modulation, Phys. Rev. Appl. **10**, 054066 (2018).
[26] J. Chen, J. Xiao, D. Lisevych, A. Shakouri, and Z. Fan, Deep-subwavelength control of acoustic waves in an ultra-compact metasurface lens, Nat. Commun. **9**, 4920 (2018).
[27] S.-W. Fan, S.-D. Zhao, A.-L. Chen, Y.-F. Wang, B. Assouar, and Y.-S. Wang, Tunable Broadband Reflective Acoustic Metasurface, Phys. Rev. Appl. **11**, 044038 (2019).
[28] S.-W. Fan, S.-D. Zhao, L. Cao, Y. Zhu, A.-L. Chen, Y.-F. Wang, K. Donda, Y.-S. Wang, and B. Assouar, Reconfigurable curved metasurface for acoustic cloaking and illusion, Phys. Rev. B **101**, 024104 (2020).
[29] J. He, X. Jiang, H. Zhao, C. Zhang, Y. Zheng, C. Liu, and D. Ta, Broadband three-dimensional focusing for an ultrasound scalpel at megahertz frequencies, Phys. Rev. Appl. **16**, 024006 (2021).
[30] L. Fan and J. Mei, Multifunctional Waterborne Acoustic Metagratings: From Extraordinary Transmission to Total and Abnormal Reflection, Phys. Rev. Appl. **16**, 044029 (2021).
[31] W. K. Cao, C. Zhang, L. T. Wu, K. Q. Guo, J. C. Ke, T. J. Cui, and Q. Cheng, Tunable Acoustic Metasurface for Three-Dimensional Wave Manipulations, Phys. Rev. Appl. **15**, 024026 (2021).
[32] H. Yang, X. Cao, F. Yang, J. Gao, S. Xu, M. Li, X. Chen, Y. Zhao, Y. Zheng, and S. Li, A programmable metasurface with dynamic polarization, scattering and focusing control, Sci. Rep. **6**, 35692 (2016).
[33] B. Assouar, B. Liang, Y. Wu, Y. Li, J.-C. Cheng, and Y. Jing, Acoustic metasurfaces, Nat. Rev. Mater. **3**, 460 (2018).
[34] Z. Hu, Z. An, Y. Kong, G. Lian, and X. Wang, The nonlinear S0 Lamb mode in a plate with a linearly-varying thickness, Ultrasonics **94**, 102 (2019).
[35] D.-C. Chen, X.-F. Zhu, D.-J. Wu, and X.-J. Liu, Broadband Airy-like beams by coded acoustic metasurfaces, Appl. Phys. Lett. **114**, 053504 (2019).
[36] D.-C. Chen, X.-F. Zhu, Q. Wei, D.-J. Wu, and X.-J. Liu, Broadband acoustic focusing by Airy-like beams based on acoustic metasurfaces, J. Appl. Phys. **123**, 044503 (2018).
[37] Y. Zhu, J. Hu, X. Fan, J. Yang, B. Liang, X. Zhu, and J. Cheng, Fine manipulation of sound via lossy metamaterials with independent and arbitrary reflection amplitude and phase, Nat. Commun. **9**, 1632 (2018).
[38] Y. Zhang, H. Cheng, J. Tian, and S. Chen, Frequency-Selected Bifunctional Coding Acoustic Metasurfaces, Phys. Rev. Appl. **14**, 064057 (2020).
[39] Y. Li, X. Jiang, B. Liang, J. C. Cheng, and L. Zhang, Metascreen-Based Acoustic Passive Phased Array, Phys. Rev. Appl. **4**, 024003 (2015).
[40] J. Qian, B.-Y. Liu, H.-X. Sun, S.-Q. Yuan, and X.-Z. Yu, Broadband acoustic focusing by symmetric Airy beams with phased arrays comprised of different numbers of cavity structures, Chin. Phys. B **26**, 114304 (2017).
[41] M. H. Fakheri, H. Rajabalipanah, and A. Abdolali, Spatiotemporal Binary Acoustic Metasurfaces, Phys. Rev. Appl. **16**, 024062 (2021).
[42] B. Xie, K. Tang, H. Cheng, Z. Liu, S. Chen, and J. Tian, Coding acoustic metasurfaces, Adv. Mater. **29**, 1603507 (2017).
[43] N. K. Efremidis, D. N. Christodoulides, I. Chremmos, and Z. Chen, Abruptly autofocusing waves, Opt. InfoBase Conf. Pap. **35**, 4045 (2011).
[44] D. G. Papazoglou, N. K. Efremidis, D. N. Christodoulides, and S. Tzortzakis, Observation of abruptly autofocusing waves, Opt. Lett. **36**, 1842 (2011).
[45] Z. Lin, X. Guo, J. Tu, Q. Ma, J. Wu, and D. Zhang, Acoustic non-diffracting Airy beam, J. Appl. Phys. **117**, 104503 (2015).
[46] N. Jiménez, V. Romero-García, V. Pagneux, and J.-P. Groby, Quasiperfect absorption by subwavelength acoustic panels in transmission using accumulation of resonances due to slow sound, Phys. Rev. B **95**, 014205 (2017).
[47] D. Tarrazó-Serrano, S. Pérez-López, P. Candelas, A. Uris, and C. Rubio, Acoustic focusing enhancement in Fresnel zone plate lenses, Sci. Rep. **9**, 7067 (2019).
[48] S. Jiménez-Gambín, N. Jiménez, J. M. Benlloch, and F. Camarena, Holograms to Focus Arbitrary Ultrasonic Fields through the Skull, Phys. Rev. Appl. **12**, 014016 (2019).
[49] F. Lu, L. Tan, Z. Tan, H. Wu, and Y. Liang, dynamical power flow and trapping-force properties of two-dimensional Airy-beam superpositions, Phys. Rev. A **104**, 023526 (2021).
[50] B. E. Treeby and B. T. Cox, K-wave: MATLAB toolbox for the simulation and reconstruction of photoacoustic wave fields, J. Biomed. Opt. **15**, 021314 (2010).
[51] T. Y. Park, K. J. Pahk, and H. Kim, Method to optimize the placement of a single-element transducer for transcranial focused ultrasound, Comput. Methods Programs Biomed. **179**, 104982 (2019).

[52] N. Wu, G. Shen, X. Qu, H. Wu, S. Qiao, E. Wang, Y. Chen, and H. Wang, an efficient and accurate parallel hybrid acoustic signal correction method for transcranial ultrasound, Phys. Med. Biol. **65**, 215019 (2020).

[53] Z. Hu, L. Xu, C.-Y. Chien, Y. Yang, Y. Gong, D. Ye, C. P. Pacia, and H. Chen, 3D transcranial microbubble cavitation localization by four sensors, IEEE Trans. Ultrason. Ferroelectr. Freq. Control **68**, 3336 (2021).

[54] S. Kim, Y. Jo, G. Kook, C. Pasquinelli, H. Kim, K. Kim, H. S. Hoe, Y. Choe, H. Rhim, A. Thielscher, *et al.*, Transcranial focused ultrasound stimulation with high spatial resolution, Brain Stimul. **14**, 290 (2021).

[55] Y.-X. Shen, Y.-G. Peng, F. Cai, K. Huang, D.-G. Zhao, C.-W. Qiu, H. Zheng, and X.-F. Zhu, Ultrasonic superoscillation wave-packets with an acoustic meta-lens, Nat. Commun. **10**, 3411 (2019).

[56] J. Li, A. Crivoi, X. Peng, L. Shen, Y. Pu, Z. Fan, and S. A. Cummer, Three dimensional acoustic tweezers with vortex streaming, Commun. Phys. **4**, 113 (2021).

[57] W. Legon, L. Ai, P. Bansal, and J. K. Mueller, Neuromodulation with single-element transcranial focused ultrasound in human thalamus, Hum. Brain Mapp. **39**, 1995 (2018).

[58] T. Li, H. Chen, T. Khokhlova, Y.-N. Wang, W. Kreider, X. He, and J. H. Hwang, Passive cavitation detection during pulsed HIFU exposures of ex vivo tissues and in vivo mouse pancreatic tumors, Ultrasound Med. Biol. **40**, 1523 (2014).

[59] Y. Zhang, J.-F. Aubry, J. Zhang, Y. Wang, J. Roy, J. F. Mata, W. Miller, E. Dumont, M. Xie, K. Lee, *et al.*, Defining the optimal age for focal lesioning in a rat model of transcranial HIFU, Ultrasound Med. Biol. **41**, 449 (2015).

[60] H. Chen and E. E. Konofagou, The size of blood-brain barrier opening induced by focused ultrasound is dictated by the acoustic pressure, J. Cereb. Blood Flow Metab. **34**, 1197 (2014).

[61] N. Lipsman, Y. Meng, A. J. Bethune, Y. Huang, B. Lam, M. Masellis, N. Herrmann, C. Heyn, I. Aubert, A. Boutet, *et al.*, Blood–brain barrier opening in Alzheimer's disease using MR-guided focused ultrasound, Nat. Commun. **9**, 2336 (2018).

[62] K.-T. Chen, W.-Y. Chai, Y.-J. Lin, C.-J. Lin, P.-Y. Chen, H.-C. Tsai, C.-Y. Huang, J. S. Kuo, H.-L. Liu, and K.-C. Wei, Neuronavigation-guided focused ultrasound for transcranial blood-brain barrier opening and immunostimulation in brain tumors, Sci. Adv. **7**, 6 (2021).

[63] Z. Hu, S. Chen, Y. Yang, Y. Gong, and H. Chen, An affordable and easy-to-use focused ultrasound device for noninvasive and high precision drug delivery to the mouse brain, IEEE Trans. Biomed. Eng. **9294**, 1 (2022).

[64] L. Zhu, G. Cheng, D. Ye, A. Nazeri, Y. Yue, W. Liu, X. Wang, G. P. Dunn, A. A. Petti, E. C. Leuthardt, *et al.*, Focused ultrasound-enabled brain tumor liquid biopsy, Sci. Rep. **8**, 6553 (2018).

[65] Y. Meng, C. B. Pople, S. Suppiah, M. Llinas, Y. Huang, A. Sahgal, J. Perry, J. Keith, B. Davidson, C. Hamani, *et al.*, MR-guided focused ultrasound liquid biopsy enriches circulating biomarkers in patients with brain tumors, Neuro. Oncol. **23**, 1789 (2021).

[66] C. P. Pacia, J. Yuan, Y. Yue, L. Xu, A. Nazeri, R. Desai, H. M. Gach, X. Wang, M. R. Talcott, A. A. Chaudhuri, *et al.*, Sonobiopsy for minimally invasive, spatiotemporally-controlled, and sensitive detection of glioblastoma-derived circulating tumor DNA, Theranostics **27**, 362 (2022).